Supplementary Materials for

Strong, lightweight, and recoverable three-dimensional ceramic nanolattices

Lucas R. Meza, Satyajit Das, Julia R. Greer*

*Corresponding author. E-mail: jrgreer@caltech.edu

Published 12 September 2014, *Science* **345**, 1322 (2014)
DOI: 10.1126/science.1255908

This PDF file includes:

Other Supporting Online Material for this manuscript includes the following:
(available at www.sciencemag.org/content/345/6202/1322/suppl/DC1)

Materials and Methods

Fabrication

Octet-truss polymer nanolattice scaffolds are written using a two photon lithography direct laser writing process in IP-Dip photoresist using the Photonic Professional lithography system (Nanoscribe GmbH). Structures are written using laser powers in a range from 6-14mW and a writing speed of ~50μm/s. The laser power is used to control the diameter of the tubes, and the speed varies slightly during the writing process to control the quality of the structure.

After a polymer scaffold is created, the structures are conformally coated in alumina using atomic layer deposition (ALD). ALD allows for the deposition of conformal coatings on complex 3D geometries with angstrom-level thickness control, resulting in high quality finished structures (*1*, *33*). Deposition is done at 150°C in a Cambridge Nanotech S200 ALD system using the following steps: H_2O is pulsed for 15ms, the system is purged for 20s, trimethyl aluminum (TMA) is pulsed for 15ms, the system is purged for 20s, and the process is repeated. The carrier gas is nitrogen, which is used at a flow rate of 20sccm (standard cubic centimeters per minute). The process was cycled for between 100 and 600 cycles to obtain the desired thickness coatings on the nanolattices. The thickness of the coatings was verified using spectroscopic ellipsometry with an alpha-SE Ellipsometer (J.A. Wollam Co., Inc.).

After deposition, two outer edges of the coated nanolattice are removed using focused ion beam (FIB) milling in an FEI Nova 200 Nanolab system in order to expose the polymer to air. Once the polymer is exposed, the samples are placed into an O_2 plasma barrel asher for between 50-75 hours, depending on the overall size of the sample, with a 300sccm flow rate of O_2 under 100W of power in order to fully remove the polymer. Structures that had been etched were cut open using FIB milling to ascertain whether the polymer had been fully removed (Fig. S5B and C). It is also possible to discern the amount of polymer that has been etched away by looking at the change in contrast of the nanolattices (Fig. S5A).

Supplementary Text

Failure Mode Formulation

The failure of the structure will originate from a combination of three potential mechanisms: fracture, Euler (beam) buckling, or local (shell) buckling. These failure modes can be defined respectively from (*28*) as

$$\sigma_{fracture} = \sigma_{fs} \tag{S1}$$

$$\sigma_{buckle} = \frac{\pi^2 EI}{(kL)^2 A_{tube}} \tag{S2}$$

$$\sigma_{shell} = \frac{E}{\sqrt{3(1-\nu^2)}}\left(\frac{t}{r_c}\right) \tag{S3}$$

Here, σ_{fs}, E, and ν are the fracture strength, Young's modulus, and Poisson's ratio of the constituent solid alumina respectively. The values L and t are the length and wall thickness of the beams. k is a constant based on the boundary condition, which, for the stretching dominated geometry used here, can be taken to be 1/2 for a pinned-pinned boundary. I and A_{tube} are the area moment of inertia and cross sectional area respectively. Taking the beams to be elliptical with a major and minor axis of a and b respectively, we can find a first order approximation of these parameters to be

$$I = \frac{\pi}{4}(3a+b)b^2 t \tag{S4}$$

$$A_{tube} = \pi(a+b)t \tag{S5}$$

r_c is the radius of curvature of the elliptical beam, which varies from $r_c = a^2/b$ to $r_c = b^2/a$, depending on the position along the ellipse. The initiation point for shell buckling will occur where $\sigma_{shell}/\sigma_{local}$ is at a maximum, meaning it will happen at the highest local stress concentration with the smallest local radius of curvature. The largest radius of curvature is at the minor axis of the ellipse, and the maximum stress, which arises from a combination of uniaxial compression and vertical bending, concentrates toward the major axes of the ellipse. To simplify the analysis, the radius of curvature at the point of shell buckling will be approximated here to be $r_c = a$ given the distribution of stresses in the beams. The diagonal tubes of the nanolattice are elliptical with an aspect ratio of ~3:1 ($a = 3b$). From this, the buckling failure criteria of the beams can be derived in terms of the major axis a of the ellipses to be

$$\sigma_{buckle} = \pi^2 E\left(\frac{3a+b}{a+b}\right)\left(\frac{b}{L}\right)^2 = \frac{5}{18}\pi^2 E\left(\frac{a}{L}\right)^2 \tag{S6}$$

$$\sigma_{shell} = \frac{E}{\sqrt{3(1-\nu^2)}}\left(\frac{t}{a}\right) \tag{S7}$$

For the nanolattice structures, there are two competing sets of failure modes: yielding vs shell buckling, and yielding vs Euler buckling. These competing modes can act independently or in combination. Yielding of the tubes will occur in tension, and

Euler and shell buckling will occur in compression. In an idealized pin-jointed stretching-dominated structure, the beams are assumed to only experience uniaxial tensile or compressive stresses, and it is the stretching of the horizontal members in tension that will govern the strength and stiffness of the lattice (*20*) (Fig. S6A). When the tubes are made to be hollow, load transfer at the nodes is governed by shell wall bending, and the resulting bending and ovalisation of the beam near the node will govern the strength and stiffness. A simplified representation of the stress concentrations that arise due to the hollow nodes is shown in Figure S6B.

If we assume that the compressive stresses and tensile stressed generated in the sample are roughly equal, which is reasonable for a beam in bending, we can find a critical transition between the modes by setting the failure equations equal to each other. From this, we can find the critical transition values to be

$$\sigma_{fracture} = \sigma_{shell} \rightarrow \boxed{\left(\frac{t}{a}\right)_{crit} = \frac{\sigma_{fs}}{E}\sqrt{3(1-\nu^2)}} \tag{S8}$$

$$\sigma_{fracture} = \sigma_{buckle} \rightarrow \boxed{\left(\frac{a}{L}\right)_{crit} = \frac{3}{\pi}\sqrt{\frac{2}{5}\frac{\sigma_{fs}}{E}}} \tag{S9}$$

It can be seen that both of these relations are functions only of the constituent properties of the materials. If we take the mechanical properties of ALD alumina found experimentally to be E = 165 *GPa*, σ_{fs} = 1.57 – 2.56 *GPa*, and ν = 0.24 (*27*), we can see that the critical shell buckling transition is $t/a \approx 0.0161 – 0.0262$, and the Euler buckling transition is $a/L \approx 0.0591 – 0.0755$. Given these bounds, the predicted failure mode for each of the structures is listed in Table S1 below.

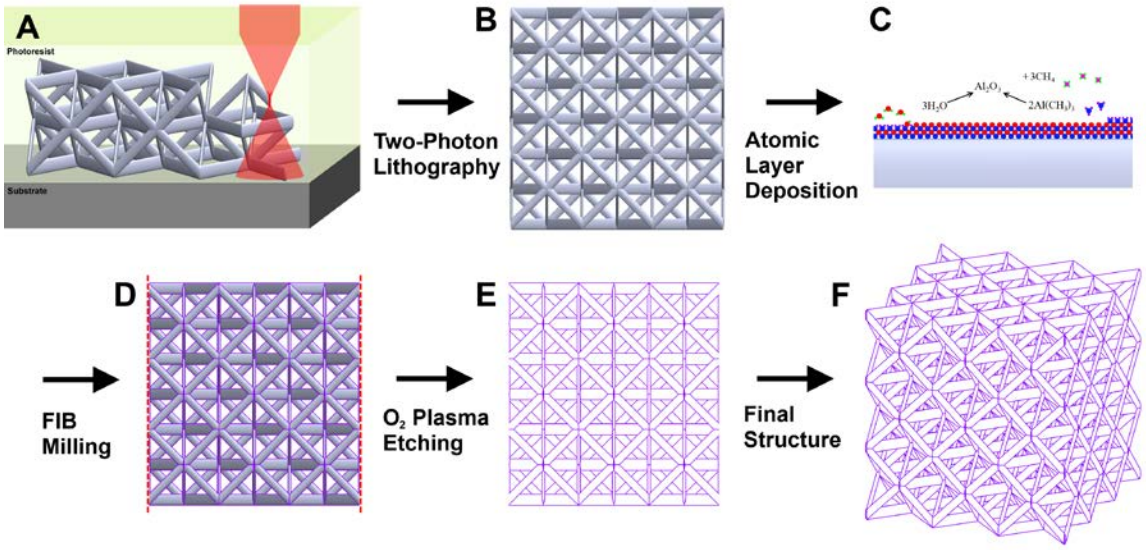

Fig. S1.

Schematic of the fabrication process for the alumina nanolattices. (A-B) Structures are written into a photopolymer using two-photon lithography. (C) Polymer scaffold is coated in alumina using ALD. (D) Coated structure is FIB milled to expose polymer. (E) Structure is exposed to O_2 plasma to remove polymer. (F) Finished free standing hollow lattice structure.

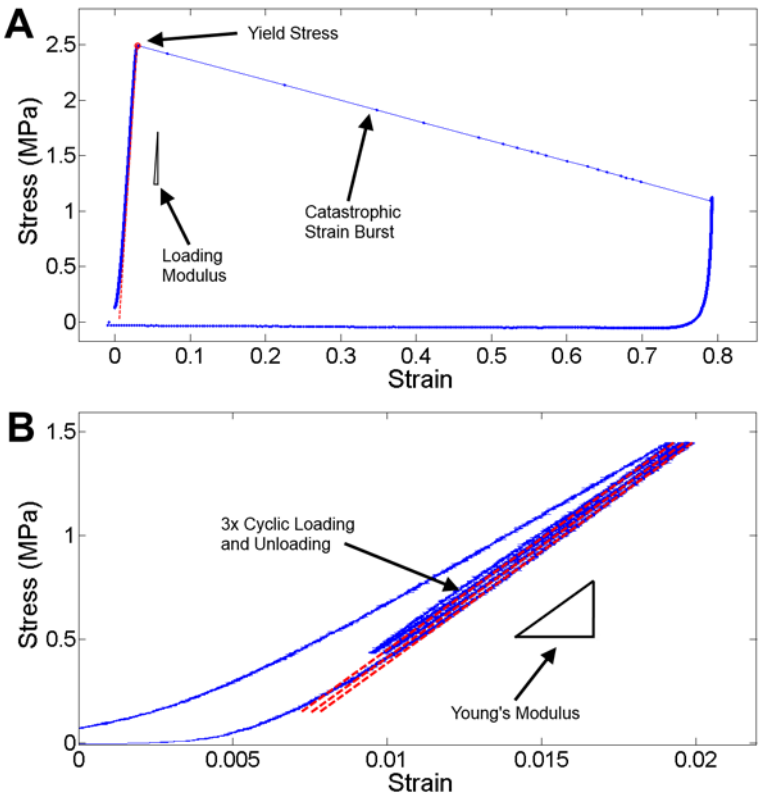

Fig. S2

Representative stress-strain curves of nanolattice compression experiments. (A) Example of one of the compression experiments on a thick-walled nanolattice showing the loading slope, the yield strength, and the deformation characteristic. (B) Example of a cyclic loading test on a nanolattice showing the unloading modulus fit used to measure the Young's modulus.

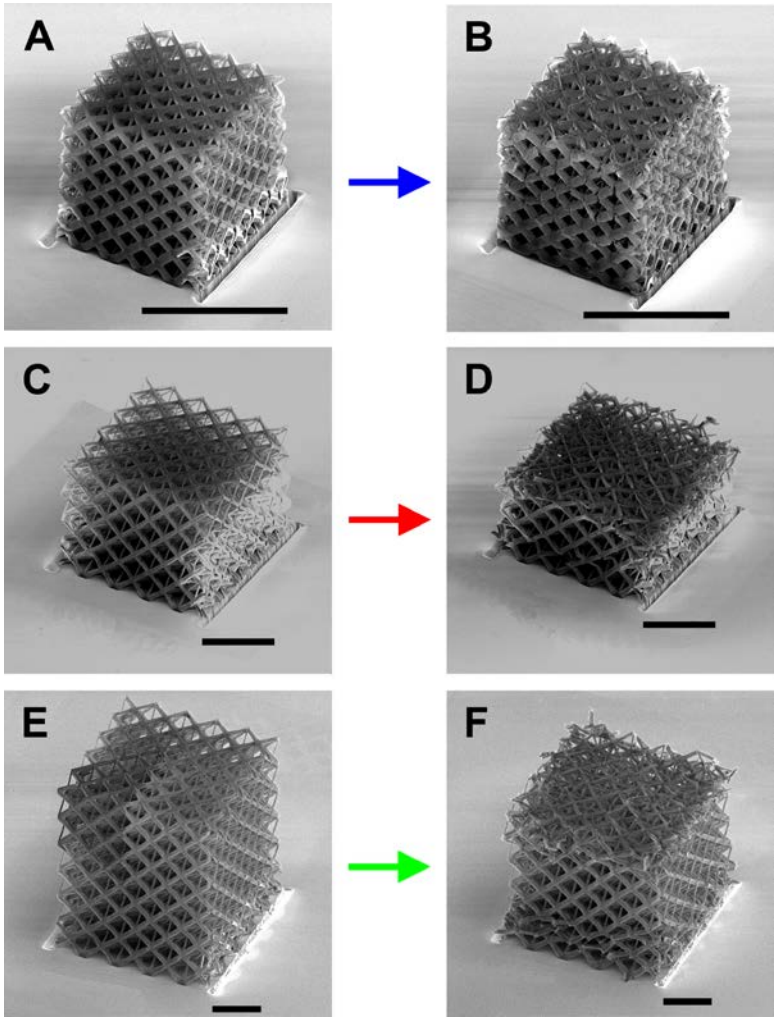

Fig. S3

Post-compression recovery of thin-walled alumina nanolattices with varying unit cell sizes. (A,B) L = 5µm, a = 650nm, t = 10nm, (C,D) L = 10µm, a = 650nm, t = 10nm, (E,F) L = 15µm, a = 1.2µm, t = 10nm

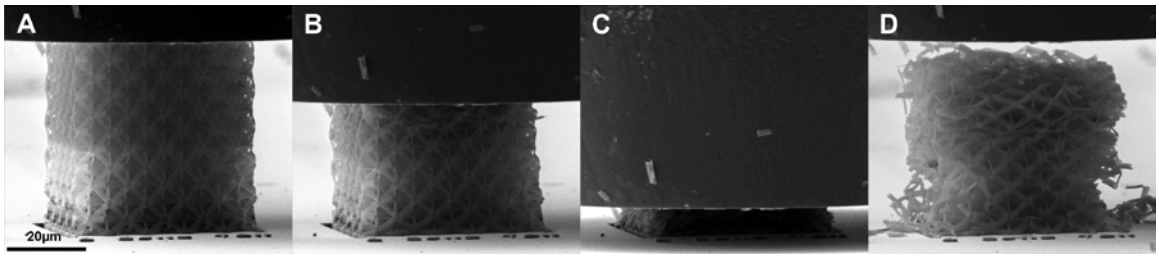

Fig. S4

Compression of a thin-walled nanolattice (L=10µm, a=750nm, t=10nm) (A) Pre-compression, (B) 35% strain, (C) 85% strain, and (D) post-compression recovered nanolattice.

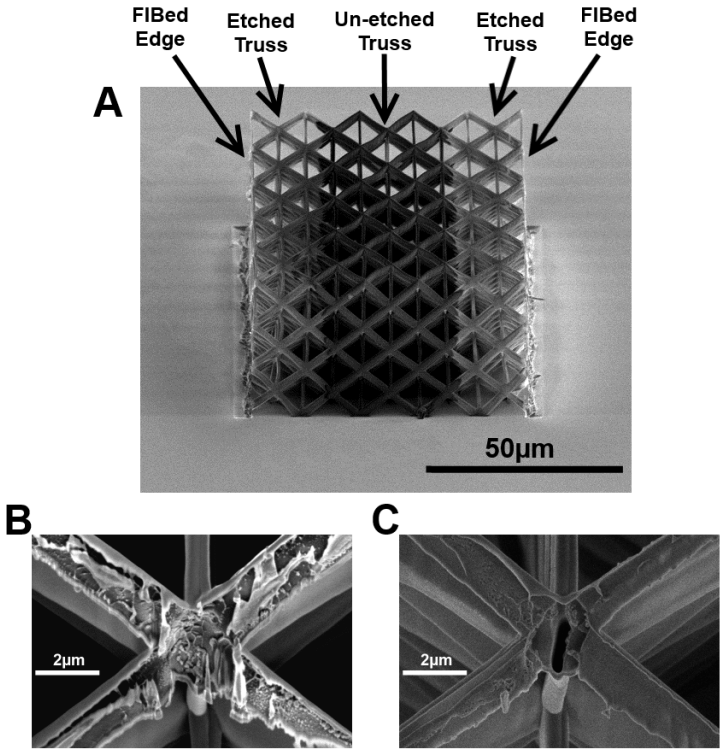

Fig. S5

Illustration of the nanolattice etching process. (A) Half-etched nanolattice showing the contrast change of the etched vs unetched portions. (B) Cross section from the partially etched section of the structure. (C) Cross section of the fully etched section of the structure.

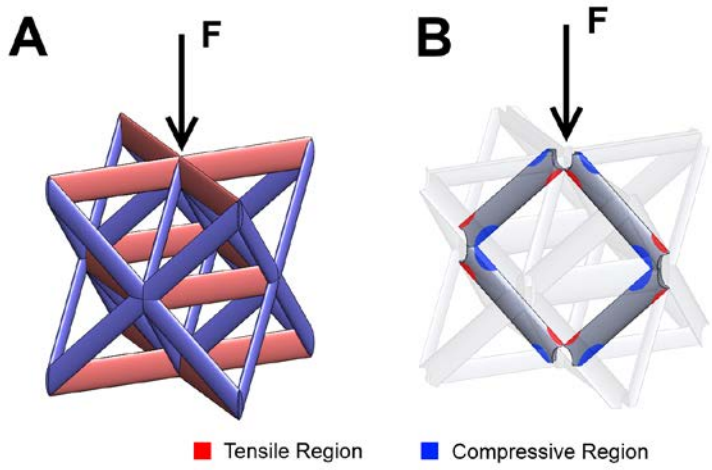

Fig. S6

Simplified representation of stress state in nanolattices. (A) Idealized stress state in a solid tube, pin-jointed lattice structure. (B) Schematic representation of stress state in a hollow tube lattice structure arising due to bending of the hollow beams near the nodes.

Table S1

List of structures fabricated, their relative densities, and *t/a* and *a/L* ratios.

Unit Cell Size *L* (μm)	Wall Thickness *t* (nm)	Tube Major Axis *a* (nm)	Relative Density	t/a	a/L	Predicted Failure Mode
5	5	535	0.0052	0.0093	0.1070	
		745	**0.0066**	**0.0067**	**0.1490**	**Shell Buckling**
	10	540	0.0105	0.0185	0.1080	
		650	**0.0120**	**0.0154**	**0.1300**	**Shell Buckling**
		750	**0.0132**	**0.0133**	**0.1500**	**Shell Buckling**
	20	450	0.0181	0.0444	0.0900	
		550	0.0212	0.0364	0.1100	Yielding
		660	0.0242	0.0303	0.1320	Yielding
		760	*0.0265*	*0.0263*	*0.1520*	*Yielding*
		860	*0.0285*	*0.0233*	*0.1720*	*Yielding*
	30	560	0.0320	0.0536	0.1120	
		670	0.0365	0.0448	0.1340	Yielding
		770	0.0399	0.0390	0.1540	Yielding
	40	570	0.0429	0.0702	0.1140	
		680	0.0488	0.0588	0.1360	Yielding
		780	0.0534	0.0513	0.1560	Yielding
	50	580	0.0541	0.0862	0.1160	
		690	0.0612	0.0725	0.1380	Yielding
		790	0.0668	0.0633	0.1580	Yielding
	60	700	0.0739	0.0857	0.1400	
		800	0.0804	0.0750	0.1600	Yielding
		900	0.0859	0.0667	0.1800	Yielding
10	5	745	0.0019	0.0067	0.0745	
		845	**0.0021**	**0.0059**	**0.0845**	**Shell Buckling**
	10	650	0.0035	0.0154	0.0650	
		750	**0.0039**	**0.0133**	**0.0750**	**Shell Buckling**
		850	**0.0044**	**0.0118**	**0.0850**	**Shell Buckling**
	20	660	0.0071	0.0303	0.0660	
		760	*0.0079*	*0.0263*	*0.0760*	*Yielding*
		860	*0.0087*	*0.0233*	*0.0860*	*Yielding*
		960	*0.0096*	*0.0208*	*0.0960*	*Yielding*
	30	770	0.0120	0.0390	0.0770	
		870	0.0132	0.0345	0.0870	Yielding
		970	0.0145	0.0309	0.0970	Yielding
	40	680	0.0142	0.0588	0.0680	
		780	0.0161	0.0513	0.0780	Yielding
		880	0.0178	0.0455	0.0880	Yielding
	50	690	0.0180	0.0725	0.0690	
		790	0.0202	0.0633	0.0790	Yielding
		890	0.0223	0.0562	0.0890	Yielding
	60	700	0.0218	0.0857	0.0700	
		800	0.0244	0.0750	0.0800	Yielding
		900	0.0269	0.0667	0.0900	Yielding
15	10	1210	0.0028	0.0083	0.0807	
		1330	**0.0030**	**0.0075**	**0.0887**	**Shell Buckling**
	20	1100	0.0051	0.0182	0.0733	
		1340	**0.0060**	**0.0149**	**0.0893**	**Shell Buckling**
	30	970	0.0069	0.0309	0.0647	
		1230	*0.0084*	*0.0244*	*0.0820*	*Yielding*
	40	1120	0.0104	0.0357	0.0747	
		1240	0.0113	0.0323	0.0827	Yielding
	50	1250	0.0142	0.0400	0.0833	
		1370	0.0153	0.0365	0.0913	Yielding
	60	1260	0.0171	0.0476	0.0840	
		1380	0.0184	0.0435	0.0920	Yielding

Legend	**Ductile-like behavior and recovery**	*Some ductile-like behavior and minimal recovery*	Brittle failure with no recovery	Cyclically tested in elastic regime (no deformation behavior recorded)

Movie S1

In-situ compression video (played at 40x speed) of a thin-walled nanolattice (5µm unit cell, 10nm wall thickness, t/a = 0.0133) to ~40% strain. Deformation is homogenous and localized to shell buckling events near the nodes. The nanolattice demonstrates almost complete recovery after compression.

Movie S2

In-situ compression video (played at 40x speed) of a nanolattice in the transition regime between thin- and thick-walled (5µm unit cell, 20nm wall thickness, t/a = 0.0233). The nanolattice is compressed to ~55% strain. It can be seen that strain bursts are associated with brittle failure events, and ductile-like deformation coincides with local buckling in the beams. The nanolattice partially recovers after compression.

Movie S3

In-situ compression video (played at 20x speed) of a thick-walled nanolattice (5µm unit cell, 60nm wall thickness, t/a = 0.0667). There is a single strain burst event to ~85% strain correlating with the catastrophic failure of the nanolattice, and no subsequent recovery after compression.

References and Notes

1. D. Jang, L. R. Meza, F. Greer, J. R. Greer, Fabrication and deformation of three-dimensional hollow ceramic nanostructures. *Nat. Mater.* **12**, 893–898 (2013). Medline doi:10.1038/nmat3738

2. J. R. Greer, J. T. M. De Hosson, Plasticity in small-sized metallic systems: Intrinsic versus extrinsic size effect. *Prog. Mater. Sci.* **56**, 654–724 (2011). doi:10.1016/j.pmatsci.2011.01.005

3. X. W. Gu, Z. Wu, Y.-W. Zhang, D. J. Srolovitz, J. R. Greer, Microstructure versus flaw: Mechanisms of failure and strength in nanostructures. *Nano Lett.* **13**, 5703–5709 (2013). Medline doi:10.1021/nl403453h

4. D. Z. Chen, D. Jang, K. M. Guan, Q. An, W. A. Goddard 3rd, J. R. Greer, Nanometallic glasses: Size reduction brings ductility, surface state drives its extent. *Nano Lett.* **13**, 4462–4468 (2013). Medline doi:10.1021/nl402384r

5. J. Rys, L. Valdevit, T. A. Schaedler, A. J. Jacobsen, W. B. Carter, J. R. Greer, Fabrication and deformation of metallic glass micro-lattices. *Adv. Eng. Mater.* **16**, 889–896 (2014). 10.1002/adem.201300454 doi:10.1002/adem.201300454

6. L. R. Meza, J. R. Greer, Mechanical characterization of hollow ceramic nanolattices. *J. Mater. Sci.* **49**, 2496–2508 (2014). doi:10.1007/s10853-013-7945-x

7. X. Zheng, H. Lee, T. H. Weisgraber, M. Shusteff, J. DeOtte, E. B. Duoss, J. D. Kuntz, M. M. Biener, Q. Ge, J. A. Jackson, S. O. Kucheyev, N. X. Fang, C. M. Spadaccini, Ultralight, ultrastiff mechanical metamaterials. *Science* **344**, 1373–1377 (2014). doi:10.1126/science.1252291

8. J. Bauer, S. Hengsbach, I. Tesari, R. Schwaiger, O. Kraft, High-strength cellular ceramic composites with 3D microarchitecture. *Proc. Natl. Acad. Sci. U.S.A.* **111**, 2453–2458 (2014). Medline doi:10.1073/pnas.1315147111

9. A. G. Evans, Perspective on the development of high-toughness ceramics. *J. Am. Ceram. Soc.* **73**, 187–206 (1990). doi:10.1111/j.1151-2916.1990.tb06493.x

10. I.-W. Chen, L. A. Xue, Development of superplastic structural ceramics. *J. Am. Ceram. Soc.* **73**, 2585–2609 (1990). doi:10.1111/j.1151-2916.1990.tb06734.x

11. P. F. Becher, Microstructural design of toughened ceramics. *J. Am. Ceram. Soc.* **74**, 255–269 (1991). doi:10.1111/j.1151-2916.1991.tb06872.x

12. D. C. Hofmann, J. Y. Suh, A. Wiest, G. Duan, M. L. Lind, M. D. Demetriou, W. L. Johnson, Designing metallic glass matrix composites with high toughness and tensile ductility. *Nature* **451**, 1085–1089 (2008). Medline doi:10.1038/nature06598

13. E. Munch, M. E. Launey, D. H. Alsem, E. Saiz, A. P. Tomsia, R. O. Ritchie, Tough, bio-inspired hybrid materials. *Science* **322**, 1516–1520 (2008). Medline doi:10.1126/science.1164865

14. J. C. Weaver, J. Aizenberg, G. E. Fantner, D. Kisailus, A. Woesz, P. Allen, K. Fields, M. J. Porter, F. W. Zok, P. K. Hansma, P. Fratzl, D. E. Morse, Hierarchical assembly of the

siliceous skeletal lattice of the hexactinellid sponge *Euplectella aspergillum*. *J. Struct. Biol.* **158**, 93–106 (2007). Medline doi:10.1016/j.jsb.2006.10.027

15. C. E. Hamm, R. Merkel, O. Springer, P. Jurkojc, C. Maier, K. Prechtel, V. Smetacek, Architecture and material properties of diatom shells provide effective mechanical protection. *Nature* **421**, 841–843 (2003). Medline doi:10.1038/nature01416

16. M. A. Meyers, J. McKittrick, P.-Y. Chen, Structural biological materials: Critical mechanics-materials connections. *Science* **339**, 773–779 (2013). Medline doi:10.1126/science.1220854

17. L. J. Gibson, M. F. Ashby, *Cellular Solids: Structure and Properties* (Cambridge Univ. Press, Cambridge, ed. 2, 1999).

18. V. S. Deshpande, M. F. Ashby, N. A. Fleck, Foam topology: Bending versus stretching dominated architectures. *Acta Mater.* **49**, 1035–1040 (2001). doi:10.1016/S1359-6454(00)00379-7

19. S. Pellegrino, C. R. Calladine, Matrix analysis of statically and kinematically indeternimate frameworks. *Int. J. Solids Struct.* **22**, 409–428 (1986). doi:10.1016/0020-7683(86)90014-4

20. V. S. Deshpande, N. A. Fleck, M. F. Ashby, Effective properties of the octet-truss lattice material. *J. Mech. Phys. Solids* **49**, 1747–1769 (2001). doi:10.1016/S0022-5096(01)00010-2

21. T. A. Schaedler, A. J. Jacobsen, A. Torrents, A. E. Sorensen, J. Lian, J. R. Greer, L. Valdevit, W. B. Carter, Ultralight metallic microlattices. *Science* **334**, 962–965 (2011). Medline doi:10.1126/science.1211649

22. L. C. Montemayor, L. R. Meza, J. R. Greer, Design and fabrication of hollow rigid nanolattices via two-photon lithography. *Adv. Eng. Mater.* **16**, 184–189 (2014). doi:10.1002/adem.201300254

23. See the supplementary materials.

24. M. D. Groner, F. H. Fabreguette, J. W. Elam, S. M. George, Low-temperature Al_2O_3 atomic layer deposition. *Chem. Mater.* **16**, 639–645 (2004). doi:10.1021/cm0304546

25. Y. K. Akimov, Field of application of aerogels. *Instrum. Exp. Tech.* **46**, 287–299 (2003) (Review). doi:10.1023/A:1024401803057

26. L. Valdevit, A. J. Jacobsen, J. R. Greer, W. B. Carter, Protocols for the optimal design of multi-functional cellular structures: From Hypersonics to micro-architected materials. *J. Am. Ceram. Soc.* **94**, s15–s34 (2011). doi:10.1111/j.1551-2916.2011.04599.x

27. M. Berdova, T. Ylitalo, I. Kassamakov, J. Heino, P. T. Törmä, L. Kilpi, H. Ronkainen, J. Koskinen, E. Hæggström, S. Franssila, Mechanical assessment of suspended ALD thin films by bulge and shaft-loading techniques. *Acta Mater.* **66**, 370–377 (2014). doi:10.1016/j.actamat.2013.11.024

28. H. G. Allen, P. S. Bulson, *Background to Buckling* (McGraw-Hill, Berkshire, UK, 1980).

29. G. Ju, S. Kyriakides, Bifurcation and localization instabilities in cylindrical shells under bending—II. Predictions. *Int. J. Solids Struct.* **29**, 1143–1171 (1992). doi:10.1016/0020-7683(92)90140-O

30. A. Torrents, T. A. Schaedler, A. J. Jacobsen, W. B. Carter, L. Valdevit, Characterization of nickel-based microlattice materials with structural hierarchy from the nanometer to the millimeter scale. *Acta Mater.* **60**, 3511–3523 (2012). doi:10.1016/j.actamat.2012.03.007

31. L. Valdevit, S. W. Godfrey, T. Schaedler, A. J. Jacobsen, W. B. Carter, Compressive strength of hollow microlattices: Experimental characterization, modeling, and optimal design. *J. Mater. Res.* **28**, 2461–2473 (2013). doi:10.1557/jmr.2013.160

32. K. J. Maloney, C. S. Roper, A. J. Jacobsen, W. B. Carter, L. Valdevit, T. A. Schaedler, Microlattices as architected thin films: Analysis of mechanical properties and high strain elastic recovery. *APL Mater.* **1**, 022106 (2013). doi:10.1063/1.4818168

33. M. Ritala, M. Leskelä, J.-P. Dekker, C. Mutsaers, P. J. Soininen, J. Skarp, Perfectly conformal TiN and Al_2O_3 films deposited by atomic layer deposition. *Chem. Vap. Depos.* **5**, 7–9 (1999). doi:10.1002/(SICI)1521-3862(199901)5:1<7::AID-CVDE7>3.0.CO;2-J